The use of artificial compressibility to improve partitioned semi-implicit FSI coupling within the classical Chorin-Témam projection framework

Tao He[a,b,*], Tong Wang[a], Hexin Zhang[c]

[a] *Department of Civil Engineering, Shanghai Normal University, Shanghai 201418, China*
[b] *School of Engineering, University of Birmingham, Birmingham B15 2TT, UK*
[c] *School of Engineering and the Built Environment, Edinburgh Napier University, Edinburgh EH10 5DT, UK*

Abstract

Over the last decade the classical Chorin-Témam projection method has been utilized to address fluid-structure interaction in a semi-implicit manner. In previous studies the fluid projection step is fully coupled with the structural motion due to the divergence-free constraint. A set of simultaneous equations thus have to be iteratively solved. To overcome this difficulty, a simple and accurate partitioned semi-implicit coupling method is proposed based on the artificial compressibility (AC) in this paper. The iterated AC parameter decouples the pressure, end-of-step velocity and structural motion within the characteristic-based split scheme. The present approach is completely matrix-free and has unlimited access to the finite elements. Its performance is demonstrated for an oscillating bluff body subjected to uniform flows.

Keywords: Fluid-structure interaction, Semi-implicit coupling, Artificial compressibility, Projection method, CBS

1. Introduction

Since the breakthrough made by Chorin and Témam [1, 2] in the late 1960s for computational fluid dynamics, the projection method has long been regarded as a powerful tool to simulate the time-dependent, incompressible viscous fluid flows. The Chorin-Témam projection method is based upon the Helmholtz-Hodge decomposition such that the initial fluid problem degrades into a sequence of decoupled elliptic equations solved for velocity and pressure variables. As expected, the projection method widely serves as a fluid subsolver in partitioned fluid-structure interaction (FSI) simulations under the arbitrary Lagrangian-Eulerian (ALE) description [3–6]. Logically, the method sheds light on pressure segregation from the global FSI system [7].

By contrast, Fernández *et al.* [8] devised a smart use of the classical Chorin-Témam projection method for predicting hemodynamic FSI. The resultant method is referred to as the *projection-based partitioned semi-implicit coupling scheme* which characterizes an intrinsic explicit-implicit treatment. To be specific, the ALE advection-diffusion step is explicitly handled with a predicted mesh whereas the fluid projection step is implicitly coupled with the structural motion on the mesh frozen temporarily. In comparison with implicit coupling scheme, the semi-implicit coupling scheme improves numerical efficiency without affecting stability too much [8]. The semi-implicit concept has since been exploited for a variety of FSI algorithms, refer to [9] for comprehensive literature survey. Basically, partitioned semi-implicit coupling methods are grouped into two categories: projection-based and non-projection-based schemes. The present attention is paid to the former that is somewhat distinguished from the traditional three-field formulation [10].

Despite decent progress, the projection-based semi-implicit coupling algorithm remains far away from being perfect. In what follows, the relevant solution procedures are briefly recalled. A monolithic

*Corresponding author.
Email addresses: txh317@bham.ac.uk (Tao He), tongwang@shnu.edu.cn (Tong Wang), j.zhang@napier.ac.uk (Hexin Zhang)

formulation of the fluid projection step and the structural motion is cast via iteratively solving a set of linearized algebraic equations in [8]. Subsequently, a coupled pressure-interface system is established after discretizing and linearizing the fluid-structure system [11]. As a matter of fact, the semi-implicit formulation is processed into the compact form at a partly monolithic level, seen from [8, 11]. To construct the fraction-step semi-implicit scheme, the first author introduced a mass source term (MST) [4] into the pressure Poisson equation (PPE) within the characteristic-based split (CBS) scheme for those elements adhering to the interface [9, 12–14]. Notwithstanding easy-to-compute metrics, the MST is rigorously derived from the three-node triangular (T3) element. In view of the above observation, the following limitations of the projection-based partitioned semi-implicit coupling method are encountered

- Complex mathematical management and increased numerical expenditure resulting from the algebraic system;
- Heavy dependence on the finite element configuration while maintaining the fractional-step modularity.

The artificial compressibility (AC) method [15] is found a fascinating option to overcome these difficulties. The AC method modifies the continuity equation through inserting a pseudo-time derivative of pressure. The resulting perturbed equation has no physical meaning but numerical importance to the steady-state solution. For unsteady flows, the requisite is a dual-time stepping procedure which implants the pseudo-time loops into the real ones. The reader is referred to several published articles [16–18] regarding the AC-based fractional step method.

The application of the AC method to FSI is straightforward. The one-dimensional piston interacting with the compressible Euler flow was dealt with in [19]. De Jouëtte *et al.* [20] investigated the dual-time stepping algorithm for both physical ingredients, where the rigid-body resolution seems involved. Teixeira and Awruch [21] utilized the explicit AC-based scheme to work out the slightly compressible fluid flows interacting with the flexible solid. Among these studies, the AC coefficient is constant and even very large, probably rendering slow convergence rate and prohibitive time step size. For this reason, the time-varying, finite AC coefficient is advocated in researches. The test load method [22, 23] formulates analytical expressions of the AC coefficient for a straight tube. The idea behind [24] rests with the persistent estimate of the AC coefficient near the wetted interface to produce superior convergence behavior. The interface AC method is easily extended to black-box solvers [24, 25] and open-source codes [26]. On the other hand, the AC coefficient can be defined on the ground of flow velocity in tandem with a user-specified parameter [27, 28]. Obviously, the pseudo-time iterations incur expensive coupling algorithm and a tip to cure this issue contains the mergence of pseudo-time iterations and coupling subiterations [29].

In order to make possible the AC-type partitioned semi-implicit coupling algorithm, we must accommodate the PPE at the implicit coupling stage and minimize numerical efforts on a general finite element mesh. Here implicit subiterations between the fluid projection step and structural motion at each time step are considered as the pseudo-time iterations. Then a suitable AC coefficient is dynamically determined to refrain from the inferior results. The decoupled FSI system pursues a completely matrix-free, efficient computation because no couple pressure-interface system should be linearized. Despite that the way of using the AC is standard, the application of the AC to the projection-type partitioned semi-implicit coupling scheme is novel and new. The proposed approach takes advantage of good features from both AC and semi-implicit schemes. Here we focus on a rigid body oscillating in uniform flows for practical importance.

The layout of this paper is organized as follows. Section 2 depicts governing equations of the coupled FSI system. The AC-based semi-implicit coupling scheme is presented in Section 3. Numerical examples are investigated in Section 4. Concluding remarks are drawn in the final section.

2. Mathematical models

2.1. Incompressible fluid flows

Let $\Omega_t^{\mathrm{F}} \subset \mathbb{R}^2$ and $(0,\ T)$ be the fluid and temporal domains, respectively. Ω_t^{F} is bounded by Γ_t^{F} which is decomposed into three complementary subsets, i.e., the Dirichlet-type boundary $\Gamma_{\mathrm{D}}^{\mathrm{F}}$, the

Neumann-type boundary $\Gamma_{\rm N}^{\rm F}$ and the fluid-structure interface Σ. The spatial and temporal coordinates are denoted by $\mathbf{x}$ and t. The Navier-Stokes equations under the ALE description governing the incompressible fluid flows on a moving domain may be written as

$$\rho\left(\frac{\partial \mathbf{u}}{\partial t}+\mathbf{c}\cdot\nabla\mathbf{u}\right)-\nabla\cdot\boldsymbol{\sigma}=\mathbf{0}\quad\text{on}\quad\Omega_t^{\rm F}\times(0,\ T), \tag{1}$$

$$\nabla\cdot\mathbf{u}=0\quad\text{on}\quad\Omega_t^{\rm F}\times(0,\ T), \tag{2}$$

where the primitive variables are the velocity $\mathbf{u}$ and the pressure p, ρ denotes the fluid density, $\mathbf{c}=\mathbf{u}-\mathbf{w}$ is the convective velocity, $\mathbf{w}$ is the mesh velocity, $\boldsymbol{\sigma}$ is the fluid stress tensor and ∇ means the gradient operator.

The constitutive equation for a Newtonian fluid is written as

$$\boldsymbol{\sigma}=-p\mathbf{I}+2\mu\boldsymbol{\epsilon}\quad\text{and}\quad\boldsymbol{\epsilon}=\frac{1}{2}\left(\nabla\mathbf{u}+(\nabla\mathbf{u})^{\rm T}\right), \tag{3}$$

where $\mathbf{I}$ indicates the identity tensor, μ is the fluid viscosity, $\boldsymbol{\epsilon}$ is the rate-of-strain tensor and superscript T indicates transpose.

The fluid problem is completed by prescribing boundary and initial conditions below

$$\mathbf{u}=\mathbf{g}\quad\text{on}\quad\Gamma_{\rm D}^{\rm F}, \tag{4a}$$

$$\boldsymbol{\sigma}\cdot\mathbf{n}=\mathbf{h}\quad\text{on}\quad\Gamma_{\rm N}^{\rm F}, \tag{4b}$$

$$\mathbf{u}(\mathbf{x},\ 0)=\mathbf{u}^0,\ p(\mathbf{x},\ 0)=p^0\quad\text{on}\quad\Omega_0^{\rm F}, \tag{4c}$$

where $\mathbf{n}$ is the unit outward normal of $\Gamma_{\rm N}^{\rm F}$.

In order to facilitate the fluid calculation, the following dimensionless scales are defined

$$\mathbf{x}^*=\frac{\mathbf{x}}{D},\ t^*=\frac{tU}{D},\ \mathbf{u}^*=\frac{\mathbf{u}}{U},\ \mathbf{c}^*=\frac{\mathbf{c}}{U},\ p^*=\frac{p}{\rho U^2}$$

based on the free stream velocity U and the characteristic length D. By employing these scales and dropping all asterisks, the dimensionless version of the Navier-Stokes equations is obtained as follows

$$\frac{\partial \mathbf{u}}{\partial t}+\mathbf{c}\cdot\nabla\mathbf{u}-\nabla\cdot\boldsymbol{\sigma}=\mathbf{0}\quad\text{on}\quad\Omega_t^{\rm F}\times(0,\ T), \tag{5}$$

$$\nabla\cdot\mathbf{u}=0\quad\text{on}\quad\Omega_t^{\rm F}\times(0,\ T), \tag{6}$$

together with the constitutive relation

$$\boldsymbol{\sigma}=-p\mathbf{I}+\frac{1}{Re}\left(\nabla\mathbf{u}+(\nabla\mathbf{u})^{\rm T}\right), \tag{7}$$

where $Re=\rho UD/\mu$ is the Reynolds number. Eqs. (5)–(7) are tackled by the projection strategy below

Step 1: Calculate the auxiliary velocity

$$\frac{\widetilde{\mathbf{u}}-\mathbf{u}^n}{\Delta t}=-\mathbf{c}^n\cdot\nabla\mathbf{u}^n+\frac{1}{Re}\nabla^2\mathbf{u}^n, \tag{8}$$

Step 2: Update the pressure

$$\nabla^2 p^{n+1}=\frac{1}{\Delta t}\nabla\cdot\widetilde{\mathbf{u}}, \tag{9}$$

Step 3: Correct the velocity

$$\frac{\mathbf{u}^{n+1}-\widetilde{\mathbf{u}}}{\Delta t}=-\nabla p^{n+1}, \tag{10}$$

where Δt is the time step.

Necessary stabilization may be added into the above steps to suppress wiggles caused by the convection and to stabilize the pressure, such as [30, 31]. The CBS scheme [6, 32] is adopted for the fluid problem since (i) it allows for the equal velocity-pressure interpolation; (ii) its stabilization parameter is independent of the local element size; and (iii) it can work in a matrix-free way. After the temporal discretization, the standard Galerkin finite element method is employed to discretize Eqs. (8)–(10) in space.

2.2. Structural motion

We consider $\Omega_t^{\mathrm{S}}\subset\mathbb{R}^2$ a structural domain with the boundary Γ_t^{S}. A rigid structure immersed in a fluid is modeled as a spring-damper-mass system under the isotropic assumption. $\mathbf{d}=\{d_1,\ d_2,\ \theta\}^{\mathrm{T}}$ signifies the structural displacement where all components are defined at the center of gravity G, and subscripts 1, 2 and θ designates the horizontal, vertical and rotational directions (Fig. 1). Along with proper boundary and initial conditions, the equation of structural motion is formulated in the Lagrangian kinematics below

$$\begin{bmatrix} m_1 & & \\ & m_2 & \\ & & m_\theta \end{bmatrix}\ddot{\mathbf{d}}+\begin{bmatrix} c_1 & & \\ & c_2 & \\ & & c_\theta \end{bmatrix}\dot{\mathbf{d}}+\begin{bmatrix} k_1 & & \\ & k_2 & \\ & & k_\theta \end{bmatrix}\mathbf{d}=\mathbf{F}, \tag{11}$$

where the dot illuminates the time derivative, m_i, c_i and k_i stand for the mass, damping and stiffness of the structure, $\mathbf{F}=\{F_{\mathrm{D}},\ F_{\mathrm{L}},\ F_{\mathrm{M}}\}^{\mathrm{T}}$ is the fluctuating fluid force, F_{D}, F_{L} and F_{M} mean the drag, lift and pitching moment, respectively.

The compatibility condition [33] must be satisfied between the center of gravity G and the surface point P. As pictured in Fig. 1, the geometric relation between $\mathbf{d}$ and $\mathbf{d}^{\mathrm{P}}$ is written in the component form as follow

$$\begin{Bmatrix} d_1^{\mathrm{P}} \\ d_2^{\mathrm{P}} \end{Bmatrix}=\begin{Bmatrix} d_1 \\ d_2 \end{Bmatrix}+\begin{bmatrix} \cos\theta-1 & -\sin\theta \\ \sin\theta & \cos\theta-1 \end{bmatrix}\begin{Bmatrix} x_1^{\mathrm{P}} \\ x_2^{\mathrm{P}} \end{Bmatrix}, \tag{12}$$

where $\mathbf{d}^{\mathrm{P}}$ is the displacement of P and $\{x_1^{\mathrm{P}},\ x_2^{\mathrm{P}}\}^{\mathrm{T}}$ is the coordinates of P.

By differentiating Eq. (12) with respect to t, the velocity relation is expressed as

$$\begin{Bmatrix} \dot{d}_1^{\mathrm{P}} \\ \dot{d}_2^{\mathrm{P}} \end{Bmatrix}=\begin{Bmatrix} \dot{d}_1 \\ \dot{d}_2 \end{Bmatrix}+\dot{\theta}\begin{bmatrix} -\sin\theta & -\cos\theta \\ \cos\theta & -\sin\theta \end{bmatrix}\begin{Bmatrix} x_1^{\mathrm{P}} \\ x_2^{\mathrm{P}} \end{Bmatrix}=\begin{bmatrix} 1 & 0 & -L_2^{\mathrm{P}} \\ 0 & 1 & L_1^{\mathrm{P}} \end{bmatrix}\begin{Bmatrix} \dot{d}_1 \\ \dot{d}_2 \\ \dot{\theta} \end{Bmatrix}, \tag{13}$$

where $L_1^{\mathrm{P}}=x_1^{\mathrm{P}}\cos\theta-x_2^{\mathrm{P}}\sin\theta$ and $L_2^{\mathrm{P}}=x_1^{\mathrm{P}}\sin\theta+x_2^{\mathrm{P}}\cos\theta$ are the angle-dependent coefficients. Similarly, the following acceleration relation is obtained by differentiating Eq. (13) in terms of time

$$\begin{aligned}\begin{Bmatrix} \ddot{d}_1^{\mathrm{P}} \\ \ddot{d}_2^{\mathrm{P}} \end{Bmatrix}&=\begin{Bmatrix} \ddot{d}_1 \\ \ddot{d}_2 \end{Bmatrix}+\ddot{\theta}\begin{bmatrix} -\sin\theta & -\cos\theta \\ \cos\theta & -\sin\theta \end{bmatrix}\begin{Bmatrix} x_1^{\mathrm{P}} \\ x_2^{\mathrm{P}} \end{Bmatrix}+\dot{\theta}^2\begin{bmatrix} -\cos\theta & \sin\theta \\ -\sin\theta & -\cos\theta \end{bmatrix}\begin{Bmatrix} x_1^{\mathrm{P}} \\ x_2^{\mathrm{P}} \end{Bmatrix}\\ &=\begin{bmatrix} 1 & 0 & -L_2^{\mathrm{P}} \\ 0 & 1 & L_1^{\mathrm{P}} \end{bmatrix}\begin{Bmatrix} \dot{d}_1 \\ \dot{d}_2 \\ \dot{\theta} \end{Bmatrix}-\begin{bmatrix} L_1^{\mathrm{P}} \\ L_2^{\mathrm{P}} \end{bmatrix}\dot{\theta}^2.\end{aligned} \tag{14}$$

The dimensionless scales

$$\mathbf{x}^*=\frac{\mathbf{x}}{D},\ t^*=\frac{tU}{D},\ d_1^*=\frac{d_1}{D},\ d_2^*=\frac{d_2}{D},$$

$$C_{\mathrm{D}} = \frac{2F_{\mathrm{D}}}{\rho U^2 D},\ C_{\mathrm{L}} = \frac{2F_{\mathrm{L}}}{\rho U^2 D},\ C_{\mathrm{M}} = \frac{2F_{\mathrm{M}}}{\rho U^2 D^2},$$
$$m_1^* = \frac{m_1}{\rho D^2},\ m_2^* = \frac{m_2}{\rho D^2},\ m_\theta^* = \frac{m_\theta}{\rho D^4}$$

and the reduced parameters

$$\xi_1 = \frac{c_1}{2\sqrt{m_1 k_1}},\ \xi_2 = \frac{c_2}{2\sqrt{m_2 k_2}},\ \xi_\theta = \frac{c_\theta}{2\sqrt{m_\theta k_\theta}},$$
$$f_{\mathrm{R}1} = \frac{f_{\mathrm{N}1} D}{U},\ f_{\mathrm{R}2} = \frac{f_{\mathrm{N}2} D}{U},\ f_{\mathrm{R}\theta} = \frac{f_{\mathrm{N}\theta} D}{U},$$
$$f_{\mathrm{N}1} = \frac{1}{2\pi}\sqrt{\frac{k_1}{m_1}},\ f_{\mathrm{N}2} = \frac{1}{2\pi}\sqrt{\frac{k_2}{m_2}},\ f_{\mathrm{N}\theta} = \frac{1}{2\pi}\sqrt{\frac{k_\theta}{m_\theta}}$$

are computed to nondimensionalize Eq. (11), where the drag coefficient C_{D}, the life coefficient C_{L} and the moment coefficient C_{M} are the dimensionless applied forces, the mass ratio m_i^* is the dimensionless mass, ξ_i is the damping ratio, $f_{\mathrm{R}i}$ is the reduced natural frequency, and $f_{\mathrm{N}i}$ is the natural frequency. By considering the above variables without superscript asterisks, the dimensionless equation of structural motion is written as

$$\ddot{\mathbf{d}} + 4\pi \begin{bmatrix} f_{\mathrm{R}1}\xi_1 & & \\ & f_{\mathrm{R}2}\xi_2 & \\ & & f_{\mathrm{R}\theta}\xi_\theta \end{bmatrix} \dot{\mathbf{d}} + 4\pi^2 \begin{bmatrix} (f_{\mathrm{R}1})^2 & & \\ & (f_{\mathrm{R}2})^2 & \\ & & (f_{\mathrm{R}\theta})^2 \end{bmatrix} \mathbf{d} = \begin{Bmatrix} \dfrac{C_{\mathrm{D}}}{2m_1^*} \\ \dfrac{C_{\mathrm{L}}}{2m_2^*} \\ \dfrac{C_{\mathrm{M}}}{2m_\theta^*} \end{Bmatrix}. \tag{15}$$

The time marching scheme utilizes the Generalized-α method [34] to advance the structural movement in time. For this reason, the semi-discrete Eq. (15) is applied to a general mid-point within the time interval, implying that the following modified equation holds

$$\mathbf{M}\ddot{\mathbf{d}}^{n+1-\alpha_m} + \mathbf{C}\dot{\mathbf{d}}^{n+1-\alpha_f} + \mathbf{K}\mathbf{d}^{n+1-\alpha_f} = \mathbf{F}^{n+1-\alpha_f}, \tag{16}$$

where

$$\ddot{\mathbf{d}}^{n+1-\alpha_m} = (1-\alpha_m)\ddot{\mathbf{d}}^{n+1} + \alpha_m \ddot{\mathbf{d}}^{n}, \tag{17a}$$

$$\dot{\mathbf{d}}^{n+1-\alpha_f} = (1-\alpha_f)\dot{\mathbf{d}}^{n+1} + \alpha_f \dot{\mathbf{d}}^{n}, \tag{17b}$$

$$\mathbf{d}^{n+1-\alpha_f} = (1-\alpha_f)\mathbf{d}^{n+1} + \alpha_f \mathbf{d}^{n}, \tag{17c}$$

$$\mathbf{F}^{n+1-\alpha_f} = (1-\alpha_f)\mathbf{F}^{n+1} + \alpha_f \mathbf{F}^{n}. \tag{17d}$$

To set $\mathbf{d}^{n+1}$ as the single unknowns in Eq. (16), the Newmark approximations [35] to the acceleration and velocity at new time step are stated as

$$\ddot{\mathbf{d}}^{n+1} = \frac{1}{\beta\Delta t^2}(\mathbf{d}^{n+1} - \mathbf{d}^{n}) - \frac{1}{\beta\Delta t}\dot{\mathbf{d}}^{n} - \frac{1-2\beta}{2\beta}\ddot{\mathbf{d}}^{n}, \tag{18}$$

$$\dot{\mathbf{d}}^{n+1} = \frac{\gamma}{\beta\Delta t}(\mathbf{d}^{n+1} - \mathbf{d}^{n}) - \frac{\gamma-\beta}{\beta}\dot{\mathbf{d}}^{n} - \frac{\gamma-2\beta}{2\beta}\Delta t\ddot{\mathbf{d}}^{n}. \tag{19}$$

Accordingly, the generalized mid-point acceleration and velocity are given by

$$\ddot{\mathbf{d}}^{n+1-\alpha_m} = \frac{1-\alpha_m}{\beta\Delta t^2}(\mathbf{d}^{n+1} - \mathbf{d}^{n}) - \frac{1-\alpha_m}{\beta\Delta t}\dot{\mathbf{d}}^{n} - \frac{1-\alpha_m-2\beta}{2\beta}\ddot{\mathbf{d}}^{n}, \tag{20}$$

$$\dot{\mathbf{d}}^{n+1-\alpha_f} = \frac{(1-\alpha_f)\gamma}{\beta\Delta t}(\mathbf{d}^{n+1} - \mathbf{d}^n) - \frac{(1-\alpha_f)\gamma - \beta}{\beta}\dot{\mathbf{d}}^n - \frac{(\gamma - 2\beta)(1-\alpha_f)}{2\beta}\Delta t\ddot{\mathbf{d}}^n. \tag{21}$$

The time integration parameters β, γ, α_m and α_f are defined as functions of the spectral radius ρ_∞ [34], and the optimal expressions are specified by

$$\beta = \frac{1}{4}(1 - \alpha_m + \alpha_f)^2,\ \gamma = \frac{1}{2} - \alpha_m + \alpha_f,\ \alpha_m = \frac{2\rho_\infty - 1}{\rho_\infty + 1},\ \alpha_f = \frac{\rho_\infty}{\rho_\infty + 1}, \tag{22}$$

where $0 \leqslant \rho_\infty \leqslant 1$ for the desired level of numerical dissipation. In accordance with [36], $\rho_\infty = 0.1$ is prescribed throughout this paper.

2.3. Mesh deformation method

Our mesh deformation method adopts a blend of the moving submesh approach (MSA) [37] and the ortho-semi-torsional spring analogy method (OST-SAM) [38]. Its fundamental principle comprises two steps below

- The OST-SAM assimilates the triangle submesh to the structural motion;
- The MSA creates a mapping between the deformation of the coarse submesh and that of the fine fluid mesh.

Interested readers are recommended to refer to [6, 39, 40] for thorough implementation. It is worth pointing out that the present approach is capable of significantly depressing time consumption of OST-SAM, as will be shown later.

2.4. Interface conditions

In partitioned FSI calculation, the interplay between the fluid and the structure is accomplished via separately enforcing the velocity continuity and the traction equilibrium on Σ as follows

$$\mathbf{u} = \dot{\mathbf{d}} \quad \text{and} \quad \mathbf{t}^{\mathrm{F}} = \mathbf{t}^{\mathrm{S}}, \tag{23}$$

where $\mathbf{t}^{\mathrm{F}} = \boldsymbol{\sigma}^{\mathrm{F}} \cdot \mathbf{n}^{\mathrm{S}}$ and $\mathbf{t}^{\mathrm{S}} = \boldsymbol{\sigma}^{\mathrm{S}} \cdot \mathbf{n}^{\mathrm{S}}$ are the fluid and structural tractions respectively, $\mathbf{n}^{\mathrm{S}}$ represents the unit outward normal of Σ pointing from the structure to the fluid and $\mathbf{n}^{\mathrm{F}} = -\mathbf{n}^{\mathrm{S}}$. Note that the external force acting on a rigid body by its surrounding fluid is a concentrated load vector. Hence the stress equilibrium on Σ becomes

$$\int_\Sigma \mathbf{t}^{\mathrm{F}} \mathrm{d}\Gamma = \int_\Sigma \mathbf{t}^{\mathrm{S}} \mathrm{d}\Gamma \quad \text{and} \quad \int_\Sigma \Delta\mathbf{x} \times \mathbf{t}^{\mathrm{F}} \mathrm{d}\Gamma = \int_\Sigma \Delta\mathbf{x} \times \mathbf{t}^{\mathrm{S}} \mathrm{d}\Gamma, \tag{24}$$

where $\Delta\mathbf{x}$ is the distance between the surface point and the center of gravity, see Fig. 1 for reference. The geometric continuity should be supplemented owing to the dynamic mesh motion

$$\mathbf{x} = \mathbf{d} \quad \text{and} \quad \mathbf{w} = \dot{\mathbf{d}}. \tag{25}$$

Besides, Eq. (23)–(25) may be imposed by adding interfacial corrections to eliminate the time lag effect [41, 42].

2.5. PPE-based partitioned semi-implicit coupling algorithm

Following the approach proposed in [8], the projection-based partitioned semi-implicit coupling algorithm based on the PPE is described in the following fractional-step sense

Step 1: Initialize all variables

Step 2: Perform the explicit coupling phase

2.1: Extrapolate the position of the interface [43]

$$\widetilde{\mathbf{x}}_\Sigma^{n+1} = \mathbf{x}_\Sigma^n + \Delta t \left(\frac{3}{2}\dot{\mathbf{x}}_\Sigma^n - \frac{1}{2}\dot{\mathbf{x}}_\Sigma^{n-1} \right)$$

2.2: Renew the fluid mesh

2.3: Compute the intermediate velocity

$$\frac{\widetilde{\mathbf{u}}-\mathbf{u}^n}{\Delta t}+\mathbf{c}^n\cdot\nabla\mathbf{u}^n-\frac{1}{Re}\nabla^2\mathbf{u}^n=\mathbf{0}$$

Step 3: Perform the implicit coupling phase

3.1: Update the pressure

$$\nabla^2 p^{n+1}-\frac{1}{\Delta t}\nabla\cdot\widetilde{\mathbf{u}}=\mathbf{0}$$

3.2: Correct the end-of-time-step velocity

$$\frac{\mathbf{u}^{n+1}-\widetilde{\mathbf{u}}}{\Delta t}+\nabla p^{n+1}=\mathbf{0}$$

3.3: Solve the structural equation

$$\mathbf{M}\ddot{\mathbf{d}}^{n+1-\alpha_m}+\mathbf{C}\dot{\mathbf{d}}^{n+1-\alpha_f}+\mathbf{K}\mathbf{d}^{n+1-\alpha_f}=\mathbf{F}^{n+1-\alpha_f}$$

It is clearly seen that, Step 3.1 is excluded from the implicit coupling stage because the pressure update explicitly relies on the auxiliary velocity. As stated in Section 1, the previously published works do not only deprive the projection method of the modularity but also demand further mathematical managements. Besides, the transplant of the scalar term [4] into the PPE within the CBS scheme is heavily confined to the T3 element. To circumvent these deficiencies, a simple and efficient alternative algorithm is provided in the next section.

3. AC-based partitioned semi-implicit coupling algorithm

3.1. Quasi-incompressible fluid flows

Let us consider the quasi-incompressible viscous fluid flows. To utilize our in-house code with minimal revision, the non-iterative AC [16] is adopted for the fluid model. Specifically, the continuity equation (2) is modified by inserting a pressure time derivative such that

$$\frac{1}{c^2}\frac{\partial p}{\partial \tau}+\nabla\cdot\mathbf{u}=0\quad\text{on}\quad\Omega_t^{\mathrm{F}}\times(0,\ T),\tag{26}$$

where c is the AC coefficient ($c\to\infty$ for incompressible fluid flows) and τ designates the pseudo-time variable. Note that c is a variable which connects the fluid projection step to the implicit coupling phase. Here we make the pseudo-time step $\Delta\tau$ equal to the physical time step Δt. The triple loops are thus avoided in the partitioned iterative coupling scheme.

3.2. AC-CBS scheme

The AC-CBS scheme is technically a non-projection variant as the incompressibility constraint is not fulfilled. However, it is rather similar to the classical Chorin-Témam projection method and offers the footstone of our semi-implicit coupling technique. It is straightforward to elaborate the procedure of the AC-CBS scheme [32] as follows

Step 1: Calculate the auxiliary velocity

$$\widetilde{\mathbf{u}}-\mathbf{u}^n=\Delta t\left(-\mathbf{c}^n\cdot\nabla\mathbf{u}^n+\frac{1}{Re}\nabla^2\mathbf{u}^n+\frac{\Delta t}{2}\mathbf{c}^n\cdot\nabla(\mathbf{c}^n\cdot\nabla\mathbf{u}^n)\right),\tag{27}$$

Step 2: Update the pressure

$$\left(\frac{1}{c^2}\right)^n(p^{n+1}-p^n)=-\Delta t\left(\nabla\cdot\widetilde{\mathbf{u}}-\Delta t\nabla^2 p^n\right),\tag{28}$$

Step 3: Correct the velocity

$$\mathbf{u}^{n+1} - \widetilde{\mathbf{u}} = -\Delta t \left(\nabla p^n - \frac{\Delta t}{2} \mathbf{c}^n \cdot \nabla^2 p^{n+\phi} \right), \tag{29}$$

where $\phi = 1$ is selected to stabilize the last step via the updated pressure.

Further to c, it is natural to make use of the formula suggested by Nithiarasu [32, 44]. However, Nithiarasu's formula may underestimate the numerical results on this occasion as recovering real transient solution is not organized in the momentum equation. It is found that the better performance is achieved via the value locally determined from [27]

$$c^2 = \max(\varepsilon^2,\ 2.5|\mathbf{u}|^2), \tag{30}$$

where ε is typically chosen to 1. In addition, the following inequality may be respected

$$c^2 \gg \left(1 + \frac{4D}{Re}\right)^2 - 1, \tag{31}$$

for low-speed incompressible flows [18].

The boundary conditions are treated in compliance with [17, 45]: no velocity boundary condition is enforced in Step 1 while the rest are handled as usual.

3.3. The proposed algorithm

The *AC-CBS-based partitioned semi-implicit coupling algorithm* is suggested in the fashion similar to [9, 14]. Fixed-point iteration is carried out to couple the fluid projection step and the structural motion, which may be accelerated by Aitken's Δ^2 technique [46] owing to its attractive simplicity and efficiency. The procedure of the proposed semi-implicit algorithm is particularized in the following.

Step 1: Initialize all variables and set $k = 0$

Step 2: Perform the explicit coupling phase

2.1: Extrapolate the position of the interface

$$(\widetilde{\mathbf{x}}_\Sigma)_k^{n+1} = \mathbf{x}_\Sigma^n + \Delta t \left(\frac{3}{2} \dot{\mathbf{x}}_\Sigma^n - \frac{1}{2} \dot{\mathbf{x}}_\Sigma^{n-1} \right)$$

2.2: Rearrange the fluid mesh

2.3: Calculate the mesh velocity and other geometric quantities

$$\mathbf{w}_k^{n+1} = \frac{\widetilde{\mathbf{x}}_k^{n+1} - \mathbf{x}^n}{\Delta t}$$

2.4: Compute the intermediate velocity

$$\mathbf{u}_k^{n+1} - \mathbf{u}^n = \Delta t \left(-\mathbf{c}^n \cdot \nabla \mathbf{u}^n + \frac{1}{Re} \nabla^2 \mathbf{u}^n + \frac{\Delta t}{2} \mathbf{c}^n \cdot \nabla (\mathbf{c}^n \cdot \nabla \mathbf{u}^n) \right)$$

Step 3: Perform the implicit coupling phase

3.1: Set $k \leftarrow k + 1$

3.2: Assess the AC coefficient c_{k-1}^{n+1}

3.3: Update the fluid pressure

$$\left(\frac{1}{c^2} \right)_{k-1}^{n+1} (p_k^{n+1} - p^n) = -\Delta t \left(\nabla \cdot \mathbf{u}_0^{n+1} - \Delta t \nabla^2 p^n \right),$$

3.4: Correct the fluid velocity

$$\mathbf{u}_k^{n+1} - \mathbf{u}_0^{n+1} = -\Delta t \left(\nabla p^n - \frac{\Delta t}{2} \mathbf{c}^n \cdot \nabla^2 p_k^{n+1} \right)$$

3.5: Solve the structural equation

$$\left(\frac{1-\alpha_m}{\beta\Delta t^2}\mathbf{M}+\frac{(1-\alpha_f)\gamma}{\beta\Delta t}\mathbf{C}+(1-\alpha_f)\mathbf{K}\right)\mathbf{d}_k^{n+1}=(1-\alpha_f)\mathbf{F}_k^{n+1}+\alpha_f\mathbf{F}^n+$$
$$\mathbf{M}\left(\frac{1-\alpha_m}{\beta\Delta t^2}\mathbf{d}^n+\frac{1-\alpha_m}{\beta\Delta t}\dot{\mathbf{d}}^n+\frac{1-\alpha_m-2\beta}{2\beta}\ddot{\mathbf{d}}^n\right)+$$
$$\mathbf{C}\left(\frac{(1-\alpha_f)\gamma}{\beta\Delta t}\mathbf{d}^n+\frac{(1-\alpha_f)\gamma-\beta}{\beta}\dot{\mathbf{d}}^n+\frac{(1-\alpha_f)(\gamma-2\beta)}{2\beta}\Delta t\ddot{\mathbf{d}}^n\right)-\mathbf{K}\alpha_f\mathbf{d}^n$$

3.6: Estimate the interfacial residuals

$$\mathbf{g}_k=\left|\,(\mathbf{x}_\Sigma)_k^{n+1}-(\widetilde{\mathbf{x}}_\Sigma)_{k-1}^{n+1}\,\right|$$

3.7: Check the convergence and the maximum number of subiterations:
if not convergent, then go ahead; otherwise, proceed to the next time step

3.8: Relax the interface's position

$$(\widetilde{\mathbf{x}}_\Sigma)_k^{n+1}=\lambda\,(\mathbf{x}_\Sigma)_k^{n+1}+(1-\lambda)\,(\widetilde{\mathbf{x}}_\Sigma)_{k-1}^{n+1}$$

3.9: Calculate the mesh velocity as the boundary condition of the fluid projection step

$$(\mathbf{w}_\Sigma)_k^{n+1}=\frac{(\widetilde{\mathbf{x}}_\Sigma)_k^{n+1}-\mathbf{x}_\Sigma^n}{\Delta t}$$

3.10: Return

Since the mass matrices are lumped for all three steps of the AC-CBS scheme, the resulting solution procedure retains completely matrix-free. The algorithm is free from the requirement for finite element, without incorporating the MST [4, 9]. Besides, the geometric conservation law may be automatically satisfied by the stabilized finite element method, provided that the mid-point rule is applied to the mesh velocity [47]. As seen above, multiple convergence standards [5, 29] are never required for various field quantities because of the AC coefficient iterated in the implicit part. The flowchart of the developed algorithm is displayed in Fig. 2.

4. Test problems

4.1. Efficiency examination of mesh updating

This subsection carries out a simple test to disclose the efficiency of our mesh deformation method. An square box with a small block inside is meshed into 55702 T3 elements and 28251 points in Fig. 3. The box is of size 1×1 while the block's geometry is 0.2×0.2. The block is moving towards the right with a given speed of 1/200 until any T3 elements penetrates. Two submeshes with and without interior nodes are also displayed in Fig. 3.

Comparison is made among different mesh moving schemes. Fig. 4(a) indicates that the present mesh moving technique saves the considerable CPU time. Though MSA-M1 invokes the OST-SAM, its cost is nearly equal to that of MSA-M2. In Fig. 4(b) only 9 iterations per time step occur on MSA-M1 and even no iterations on MSA-M2. Moreover, the OST-SAM demands more than 440 iterations per time step and the number will mount up with the increase in time and scale.

4.2. Vortex-induced vibration of a circular cylinder

In this example an elastically mounted circular cylinder is allowed to transversely oscillate in the laminar flow region. The problem settings are schematically demonstrated in Fig. 5 where D is the diameter of the circular cylinder. The system properties are consistent with [48]: the mass ratio $m_2^*=116.37$, the damping ratio $\xi_2=1.237\times10^{-3}$, the reduced natural frequency $f_{\mathrm{R}2}=17.961/Re$ and $90\leqslant Re\leqslant140$.

For the sake of efficiency, the computational domain is divided into the Eulerian subdomain A1, the ALE subdomain A2 and the Lagrangian subdomain A3. The size of A2 is $6D\times6D$ while that of

A3 is $1.2D \times 1.2D$. The points in A1 keep fixed at all time while those in A3 move along with the cylinder. In A2 the points are continuously updated. In Fig. 6(a) the finite element mesh constitutes 8092 T3 elements and 4141 points, and the corresponding submesh is shown in Fig. 6(b). The time step is $\Delta t = 1.0 \times 10^{-2}$ and the convergence tolerance is $tol = 1.0 \times 10^{-6}$.

Two sets of finite element meshes, M1 (8092 T3 elements and 4141 points) and M2 (15856 T3 elements and 8033 points), are utilized for the mesh sensitivity evaluation. The computed results of the flow past the vibrating cylinder at $Re = 105$ are listed in Table 1, including the amplitude of vertical amplitude d_{MAX2}, the mean value of drag coefficient $C_{\mathrm{D,MEAN}}$ and its root mean square (RMS) $C_{\mathrm{D,RMS}}$, the amplitude of lift coefficient $C_{\mathrm{L,MAX}}$ and its RMS $C_{\mathrm{L,RMS}}$, the Strouhal number St and the ratio of vortex-shedding frequency f_{V} to natural frequency f_{N2}. An excellent agreement is observed between both meshes in Table 1. After examining the obtained data, the deviation is even 0.45% for the maximum amplitude in transverse oscillation. This preliminary study establishes the adequacy of M1 in computing flow past the oscillating cylinder at various Re. Similar tests are not repeated elsewhere for brevity.

The convergence behavior of the present algorithm is assessed in Fig. 7. It is seen from Fig. 7(a) that the interfacial residuals estimated by the AC-based method are quite tiny when converged, and they are slightly smaller than those from the PPE-based method. A fast convergence history is graphically plotted in Fig. 7(b). Typically, $2 \sim 3$ subiterations per time step are sufficient to reach convergence. Furthermore, Table 2 investigates the impact of convergence criterion on the $Re = 105$ flow. The convergence due to $tol = 1.0 \times 10^{-9}$ is monitored in Fig. 8 for a typical time step when the fluid flow fully develops. An excellent agreement is revealed between the two sets of converged solutions, although a more stringent tolerance asks for more subiterations at each time step. Therefore, $tol = 1.0 \times 10^{-6}$ is the better option for further computations. The comparable numbers of subiterations are reported by Baek and Karniadakis [49] in similar cases. This is because the oscillating bluff body is heavier than its surrounding fluid.

Fig. 9 further examines the residual of the pseudo-time pressure term in the modified continuity equation based on the L_2 norm [32]

$$Error = \sqrt{\overline{\frac{1}{np}\sum_{i=1}^{np}\left(\frac{1}{c_i^2}\frac{p_i^{n+1}-p_i^n}{\Delta t}\right)^2}}, \tag{32}$$

where np is the number of nodes and subscript i designates the i-th node. Fig. 9 discloses that the residual of the quasi-incompressibility is rather small in the L_2 norm, though the finite AC coefficient is dynamically evaluated at each subiteration. In this sense, the incompressibility condition is successfully recovered when the converged solution is achieved for the transient flows. In consideration of Figs. 7–9, the present AC-based semi-implicit coupling method possesses the good convergence behavior in the vibrating cylinder problem.

In Fig. 10 the amplitude d_{MAX2} and the frequency ratio $f_{\mathrm{V}}/f_{\mathrm{N2}}$ of the oscillating cylinder are inspected at various Re. For comparison, Fig. 10 is also overlaid with the $Re - St$ function [50]

$$St = 0.212 \times (1.0 - \frac{21.2}{Re}), \tag{33}$$

for a rigid circular cylinder. It is noticed that, a narrow *lock-in* range computed by [9] covers $98 \leqslant Re \leqslant 108$, which is nearly coincident with our early work [6, 12, 39, 51] and those of [36, 52–54]. On the contrary, the present method produces the widened lock-in range and the larger amplitudes during resonance. Specifically, the lock-in phenomenon starts at $Re = 99$ and ends at $Re = 115$. Key aerodynamic indicators evaluated at $Re = 100$ are listed in Table 3, exposing that the obtained data are in better agreement with the experimental research [48]. Note that at this Re lock-in is not aroused in [54]. The cylinder oscillation is very faint when Re steps out of the lower end of the lock-in region. At this point, the vortices are shedding at the Strouhal frequency lower than its natural frequency. Within the lock-in region, the frequency ratio $f_{\mathrm{V}}/f_{\mathrm{N2}}$ roams around unity, implying the synchronization of the oscillation and vortex-shedding frequencies. Such a synchronization is responsible for large-scale and strong motions of the cylinder. Different from [6, 12, 39], the smooth rise in amplitude is seen in Fig. 10. The amplitude abruptly descends once Re migrates outside the upper end of the lock-in

region. With the growth of Re, the cylinder keeps on imperceptibly oscillating and f_{V} reaches a high level.

Providing that Re is outside the lock-in region, f_{V} deviates from f_{N2} and thus it becomes unlocked. The cylinder amplitude is modulated, forming the *beating* phenomenon. Figs. 11(a) and 11(b) depicts time histories of the cylinder displacement at $Re = 97$ and 120. Different from [6], the beating phenomena are obviously modulated at both Reynolds numbers. The time history of the cylinder displacement at $Re = 105$ is displayed in Fig. 11(c) where lock-in is clearly observed. The corresponding vorticity fields for these Reynolds numbers are illustrated in Fig. 12. The cylinder undergoes low-amplitude oscillations at $Re = 97$ and 120, whereas high-amplitude oscillations are perceived at $Re = 105$. It is apparent that, compared to $Re = 105$, the vortex spacing is reduced at the other two Re. Unlike [55], the three vortex-shedding modes behind the cylinder wake are of the 2S type [56]. The associated mode seems closer to the standard 2S mode for a rigid circular cylinder. The explanation is given as follow: since the cylinder motion is very faint at these Reynolds numbers, the structural oscillation hardly alters the flow pattern as well as the vortex-shedding frequency. Hence the frequency ratio almost tallies with the Roshko curve outside the lock-in region, as shown in Fig. 10.

Another issue of interest is the numerical efficiency of our approach. The $Re = 100$ flow is chosen as the reference case. We can quantify time consumption of the PPE-based and AC-based semi-implicit coupling techniques with reference to Fig. 13. The figure fairly reports that the latter technique costs roughly 87% run time of the former one.

4.3. Flutter of a bridge deck

As an ideal example to illustrate the flutter failure of Tacoma Narrows Bridge in 1940, we present in this subsection the numerical simulation of an H-profile bridge deck. The deck model is mounted with the vertical and rotational springs so that it experiences a coupled motion of vertical translation and rotation. The representation of this problem is graphically illustrated in Fig. 14 with D being the deck's width. The system parameters are taken from [57]: the mass ratios $m_2^* = 16.667$ and $m_\theta^* = 0.976$, the damping ratios $\xi_2 = 2.041 \times 10^{-2}$ and $\xi_\theta = 3.458 \times 10^{-2}$, the reduced natural frequencies $f_{\mathrm{R}2} = 0.1559$ and $f_{\mathrm{R}\theta} = 0.2401$ and the Reynolds number $Re = 1500$.

The domain decomposition is plotted in Fig. 14 as well. The size of A2 is $4D \times 4D$, while that of A3 is $2 \times 0.95D \times 0.0875D$ comprising two rectangular parts. In the first panel of Fig. 15 the finite element mesh consists of 6486 T3 elements and 3329 points, and the corresponding submesh is demonstrated in the second panel. $\Delta t = 1.0 \times 10^{-2}$ and $tol = 1.0 \times 10^{-6}$ are utilized here.

Similarly, the convergence analysis is preformed for the oscillating deck in Fig. 16. Fig. 16(a) discloses the minute residuals of interfacial displacement within the semi-implicit coupling process. In the figure the residuals of the AC-based method are obviously smaller than those of the PPE-based method. The residuals versus the number of subiterations required to converge is drawn in Fig. 16(b). Only $2 \sim 3$ subiterations per time step are required for the stable coupling of interacting fields under the specific criterion. Seen from Table 4, the present method is insensitive to the tolerance in the deck problem. The diagram of residual reduction using $tol = 1.0 \times 10^{-9}$ is displayed in Fig. 17 as well. As a result, $tol = 1.0 \times 10^{-6}$ is the proper level of tolerance for terminating the subiterations. Compared to last example, the amount of subiterations slightly increases at each time step due to the coupled motion of two degrees of freedom.

To demonstrate the applicability of the chosen AC coefficient, the L_2-norm residual based on Eq. (32) is estimated in Fig. 18. Seen from the figure, the obtained residual sharply decreases to a very small value and maintains such a desirable level when the flow fully develops. This reality clearly explains that the incompressibility condition is indeed satisfied by the proposed method once the convergence is gained. As observed from Figs. 16–18, the solution convergence history is very good in the deck flutter as well.

The simple geometry of this problem does not mean that the comparable data can be easily acquired. We are aware that the data from [12, 36, 58–60] significantly vary in the case of zero damping. For example, Cebral and Löhner [60] gave a rather small rotation whereas a large amplitude is seen in [36]. The simulation is even terminated at $t = 55s$ in [58]. However, the difference in computed data is usually acceptable due to the demonstrated complexity of the deck flutter. Table 5 reports the vertical amplitude $d_{\mathrm{MAX}2}$, the vertical oscillation frequency $f_{\mathrm{O}2}$, the rotational amplitude $d_{\mathrm{MAX}\theta}$

and the rotational oscillation frequency $f_{O\theta}$. It is noticed that, the relative error from this paper is minimum in rotation while larger values are obtained by our previous work [9, 40]. In spite of smaller vertical amplitude, the vertical vibration is extremely weak and plays little role in the torsional flutter. The present results are reasonable, given the dominant structural rotation. We also notice that, the vertical oscillation frequency coincides with its rotational counterpart when the flutter occurs. The relevant power spectra is shown in Fig. 19 by using a fast Fourier transform on the time history of rotation.

Time histories of two displacement components of the deck are shown in Fig. 20. Apparently, this study and the PPE-based implicit coupling solver [40] reach the steady solutions at almost the same time. We notice from Table 5 and Fig. 20 that, the rotational oscillation frequency of the deck is quite close to its natural rotational frequency while the vertical oscillation is very feeble. Given the observation, the flutter phenomenon is obviously exposed here. In fact, bluff bodies in oscillatory motions shed wakes at both oscillation and Strouhal frequencies, but the deck rotation is the dominant motion in this case. The same conclusion is drawn by Lee *et al.* [61]. A typical vorticity contour is illustrated in Fig. 21. The vortex pattern over the oscillating deck agrees well with the early documented explanation [62]. Fig. 22 exhibits the numerical expenses spent by the two methods. Again, the AC-based method is in possession of approximately 20% savings in CPU time.

5. Conclusions

This paper has reported the AC-CBS-based partitioned semi-implicit FSI coupling strategy within the ALE finite element framework. The quasi-incompressible CBS scheme is used for the fluid problem whereas the structural equation is advanced in time by the Generalized-α method. The dynamic mesh is efficiently updated by means of the combination of the MSA and OST-SAM. The partitioned semi-implicit coupling algorithm is recast in terms of the AC-CBS scheme where the AC coefficient is iterated within the implicit coupling phase. The main contributions are summarized as follows

- The fractional-step implementation is very simple, accompanied by minimal programming efforts;
- The algorithm is entirely matrix-free, without solving a set of algebraic equations;
- Any finite elements are feasible for the proposed scheme.

The present method is validated against available data for two benchmark problems. Compared with its PPE-based counterpart, the AC-based method holds the better convergence behavior, without violating the incompressibility. In contrast with our earlier attempts, the predicted displacement agrees better with the well-documented data while the higher efficiency is gained in both examples. The lock-in, beating and flutter phenomena are successfully detected. Despite this presentation, more work is needed to develop the AC-based partitioned semi-implicit coupling method in the future.

Acknowledgements

Supports from National Natural Science Foundation of China under grant numbers 51508332 and 51508333 are gratefully acknowledged. The authors wish to thank the anonymous referees and Dr. M. Ricchiuto for their insightful comments in improving this paper.

References

[1] A. J. Chorin, Numerical solution of the Navier-Stokes equations, Mathematics of Computation 22 (104) (1968) 745–762.

[2] R. Témam, Une méthode d'approximation de la solution des équations de Navier-Stokes, Bulletin de la Société Mathématique de France 96 (1968) 115–152.

[3] A. Anju, A. Maruoka, M. Kawahara, 2-D fluid–structure interaction problems by an arbitrary Lagrangian-Eulerian finite element method, International Journal of Computational Fluid Dynamics 8 (1) (1997) 1–9.

[4] Y.-J. Jan, T. W.-H. Sheu, Finite element analysis of vortex shedding oscillations from cylinders in the straight channel, Computational Mechanics 33 (2) (2004) 81–94.

[5] S. Badia, R. Codina, On some fluid–structure iterative algorithms using pressure segregation methods. Application to aeroelasticity, International Journal for Numerical Methods in Engineering 72 (1) (2007) 46–71.

[6] T. He, D. Zhou, Y. Bao, Combined interface boundary condition method for fluid–rigid body interaction, Computer Methods in Applied Mechanics and Engineering 223 (2012) 81–102.

[7] P. Ryzhakov, E. Oñate, R. Rossi, S. Idelsohn, Improving mass conservation in simulation of incompressible flows, International Journal for Numerical Methods in Engineering 90 (12) (2012) 1435–1451.

[8] M. A. Fernández, J.-F. Gerbeau, C. Grandmont, A projection semi-implicit scheme for the coupling of an elastic structure with an incompressible fluid, International Journal for Numerical Methods in Engineering 69 (4) (2007) 794–821.

[9] T. He, A CBS-based partitioned semi-implicit coupling algorithm for fluid–structure interaction using MCIBC method, Computer Methods in Applied Mechanics and Engineering 298 (2016) 252–278.

[10] C. Farhat, P. Geuzaine, G. Brown, Application of a three-field nonlinear fluid–structure formulation to the prediction of the aeroelastic parameters of an F-16 fighter, Computers & Fluids 32 (1) (2003) 3–29.

[11] S. Badia, A. Quaini, A. Quarteroni, Splitting methods based on algebraic factorization for fluid–structure interaction, SIAM Journal on Scientific Computing 30 (4) (2008) 1778–1805.

[12] T. He, Partitioned coupling strategies for fluid–structure interaction with large displacement: Explicit, implicit and semi-implicit schemes, Wind & Structures 20 (3) (2015) 423–448.

[13] T. He, Semi-implicit coupling of CS-FEM and FEM for the interaction between a geometrically nonlinear solid and an incompressible fluid, International Journal of Computational Methods 12 (5) (2015) 1550025.

[14] T. He, K. Zhang, Combined interface boundary condition method for fluid–structure interaction: Some improvements and extensions, Ocean Engineering 109 (2015) 243–255.

[15] A. J. Chorin, A numerical method for solving incompressible viscous flow problems, Journal of Computational Physics 2 (1) (1967) 12–26.

[16] P. A. Madsen, H. Schäffer, A discussion of artificial compressibility, Coastal Engineering 53 (1) (2006) 93–98.

[17] H. S. Tang, F. Sotiropoulos, Fractional step artificial compressibility schemes for the unsteady incompressible Navier-Stokes equations, Computers & Fluids 36 (5) (2007) 974–986.

[18] L. Könözsy, D. Drikakis, A unified fractional-step, artificial compressibility and pressure-projection formulation for solving the incompressible Navier-Stokes equations, Communications in Computational Physics 16 (5) (2014) 1135–1180.

[19] S. Piperno, C. Farhat, B. Larrouturou, Partitioned procedures for the transient solution of coupled aroelastic problems Part I: Model problem, theory and two-dimensional application, Computer Methods in Applied Mechanics and Engineering 124 (1) (1995) 79–112.

[20] C. De Jouëtte, O. Laget, J.-M. Le Gouez, H. Viviand, A dual time stepping method for fluid–structure interaction problems, Computers & Fluids 31 (4) (2002) 509–537.

[21] P. R. F. Teixeira, A. M. Awruch, Numerical simulation of fluid-structure interaction using the finite element method, Computers & Fluids 34 (2) (2005) 249–273.

[22] P. Råback, J. Ruokolainen, M. Lyly, E. Järvinen, Fluid-structure interaction boundary conditions by artificial compressibility, in: ECCOMAS Computational Fluid Dynamics Conference, The Institute of Mathematics and its Applications, University of Wales, Swansea, UK, 2001.

[23] E. Järvinen, P. Råback, M. Lyly, J.-P. Salenius, A method for partitioned fluid–structure interaction computation of flow in arteries, Medical Engineering & Physics 30 (7) (2008) 917–923.

[24] J. Degroote, A. Swillens, P. Bruggeman, R. Haelterman, P. Segers, J. Vierendeels, Simulation of fluid–structure interaction with the interface artificial compressibility method, International Journal for Numerical Methods in Biomedical Engineering 26 (3-4) (2010) 276–289.

[25] A. E. J. Bogaers, S. Kok, B. D. Reddy, T. Franz, Extending the robustness and efficiency of artificial compressibility for partitioned fluid–structure interactions, Computer Methods in Applied Mechanics and Engineering 283 (2015) 1278–1295.

[26] M. Olivier, G. Dumas, A parametric investigation of the propulsion of 2D chordwise-flexible flapping wings at low Reynolds number using numerical simulations, Journal of Fluids and Structures 63 (2016) 210–237.

[27] C. Wood, A. J. Gil, O. Hassan, J. Bonet, Partitioned block-Gauss–Seidel coupling for dynamic fluid–structure interaction, Computers & Structures 88 (23) (2010) 1367–1382.

[28] O. F. Oxtoby, A. G. Malan, A matrix-free, implicit, incompressible fractional-step algorithm for fluid–structure interaction applications, Journal of Computational Physics 231 (16) (2012) 5389–5405.

[29] U. Küttler, C. Förster, W. A. Wall, A solution for the incompressibility dilemma in partitioned fluid–structure interaction with pure Dirichlet fluid domains, Computational Mechanics 38 (4-5) (2006) 417–429.

[30] C. H. Liu, D. Y. C. Leung, Development of a finite element solution for the unsteady Navier–Stokes equations using projection method and fractional-θ-scheme, Computer Methods in Applied Mechanics and Engineering 190 (32) (2001) 4301–4317.

[31] Y. Bao, D. Zhou, C. Huang, Numerical simulation of flow over three circular cylinders in equilateral arrangements at low Reynolds number by a second-order characteristic-based split finite element method, Computers & Fluids 39 (5) (2010) 882–899.

[32] P. Nithiarasu, An efficient artificial compressibility (AC) scheme based on the characteristic based split (CBS) method for incompressible flows, International Journal for Numerical Methods in Engineering 56 (13) (2003) 1815–1845.

[33] T. Nomura, T. J. R. Hughes, An arbitrary Lagrangian-Eulerian finite element method for interaction of fluid and a rigid body, Computer Methods in Applied Mechanics and Engineering 95 (1) (1992) 115–138.

[34] J. Chung, G. M. Hulbert, A time integration algorithm for structural dynamics with improved numerical dissipation: The Generalized-α method, Journal of Applied Mechanics–ASME 60 (2) (1993) 371–375.

[35] N. M. Newmark, A method of computation for structural dynamics, Journal of Engineering Mechanics–ASCE 85 (3) (1959) 67–94.

[36] W. Dettmer, D. Perić, A computational framework for fluid–rigid body interaction: Finite element formulation and applications, Computer Methods in Applied Mechanics and Engineering 195 (13) (2006) 1633–1666.

[37] E. Lefrançois, A simple mesh deformation technique for fluid–structure interaction based on a submesh approach, International Journal for Numerical Methods in Engineering 75 (9) (2008) 1085–1101.

[38] G. A. Markou, Z. S. Mouroutis, D. C. Charmpis, M. Papadrakakis, The ortho-semi-torsional (OST) spring analogy method for 3D mesh moving boundary problems, Computer Methods in Applied Mechanics and Engineering 196 (4) (2007) 747–765.

[39] T. He, D. Zhou, Z. Han, J. Tu, J. Ma, Partitioned subiterative coupling schemes for aeroelasticity using combined interface boundary condition method, International Journal of Computational Fluid Dynamics 28 (6-10) (2014) 272–300.

[40] T. He, On a partitioned strong coupling algorithm for modeling fluid–structure interaction, International Journal of Applied Mechanics 7 (2) (2015) 1550021.

[41] R. Jaiman, P. Geubelle, E. Loth, X. Jiao, Transient fluid–structure interaction with non-matching spatial and temporal discretizations, Computers & Fluids 50 (1) (2011) 120–135.

[42] T. He, K. Zhang, An overview of the combined interface boundary condition method for fluid–structure interaction, Archives of Computational Methods in Engineering 24 (4) (2017) 891–934.

[43] S. Piperno, Explicit/implicit fluid/structure staggered procedures with a structural predictor and fluid subcycling for 2D inviscid aeroelastic simulations, International Journal for Numerical Methods in Fluids 25 (10) (1997) 1207–1226.

[44] P. Nithiarasu, An arbitrary Lagrangian Eulerian (ALE) formulation for free surface flows using the characteristic-based split (CBS) scheme, International Journal for Numerical Methods in Fluids 48 (12) (2005) 1415–1428.

[45] R. Codina, M. Vázquez, O. C. Zienkiewicz, A general algorithm for compressible and incompressible flows. Part III: The semi-implicit form, International Journal for Numerical Methods in Fluids 27 (1-4) (1998) 13–32.

[46] D. P. Mok, W. A. Wall, Partitioned analysis schemes for the transient interaction of incompressible flows and nonlinear flexible structures, in: W. A. Wall, K.-U. Bletzinger, K. Schweizerhof (Eds.), Trends in Computational Structural Mechanics, CIMNE, Barcelona, Spain, 2001, pp. 689–698.

[47] M. Lesoinne, C. Farhat, Geometric conservation laws for flow problems with moving boundaries and deformable meshes, and their impact on aeroelastic computations, Computer Methods in Applied Mechanics and Engineering 134 (1) (1996) 71–90.

[48] P. Anagnostopoulos, P. Bearman, Response characteristics of a vortex-excited cylinder at low Reynolds numbers, Journal of Fluids and Structures 6 (1) (1992) 39–50.

[49] H. Baek, G. E. Karniadakis, A convergence study of a new partitioned fluid–structure interaction algorithm based on fictitious mass and damping, Journal of Computational Physics 231 (2) (2012) 629–652.

[50] A. Roshko, On the development of turbulent wakes from vortex streets, Technical Report NACA TN 1191, National Advisory Committee for Aeronautics (1954).

[51] T. He, A partitioned implicit coupling strategy for incompressible flow past an oscillating cylinder, International Journal of Computational Methods 12 (2) (2015) 1550012.

[52] D. L. Young, J. T. Chang, T. I. Eldho, A coupled BEM and arbitrary Lagrangian–Eulerian FEM model for the solution of two-dimensional laminar flows in external flow fields, International Journal for Numerical Methods in Engineering 51 (9) (2001) 1053–1077.

[53] A. De Rosis, G. Falcucci, S. Ubertini, F. Ubertini, S. Succi, Lattice Boltzmann analysis of fluid-structure interaction with moving boundaries, Communications in Computational Physics 13 (3) (2013) 823–834.

[54] C. Samaniego, G. Houzeaux, E. Samaniego, M. Vázquez, Parallel embedded boundary methods for fluid and rigid-body interaction, Computer Methods in Applied Mechanics and Engineering 290 (2015) 387–419.

[55] M. H. Bahmani, M. H. Akbari, Effects of mass and damping ratios on VIV of a circular cylinder, Ocean Engineering 37 (5) (2010) 511–519.

[56] C. H. K. Williamson, A. Roshko, Vortex formation in the wake of an oscillating cylinder, Journal of Fluids and Structures 2 (4) (1988) 355–381.

[57] G. Filippini, L. Dalcin, N. Nigro, M. Storti, Fluid-rigid body interaction by PETs-FEM driven by Python, Mecánica Computacional XXVII (8) (2008) 489–504.

[58] B. Hübner, E. Walhorn, D. Dinkier, Strongly coupled analysis of fluid–structure interaction using space-time finite elements, in: Proceedings of the 2nd European Conference on Computational Mechanics, Cracow, Poland, 2001, pp. 546–547.

[59] G. Fourestey, S. Piperno, A second-order time-accurate ALE Lagrange–Galerkin method applied to wind engineering and control of bridge profiles, Computer Methods in Applied Mechanics and Engineering 193 (39) (2004) 4117–4137.

[60] J. R. Cebral, R. Löhner, On the loose coupling of implicit time-marching codes, in: Proceedings of the 43th AIAA Aerospace Sciences Meeting and Exhibit, American Institute of Aeronautics and Astronautics, Reno, Nevada, USA, 2005, pp. 1–15.

[61] N. Lee, H. Lee, C. Baek, S. Lee, Aeroelastic analysis of bridge deck flutter with modified implicit coupling method, Journal of Wind Engineering and Industrial Aerodynamics 155 (2016) 11–22.

[62] K. Y. Billah, R. H. Scanlan, Resonance, Tacoma Narrows bridge failure, and undergraduate physics textbooks, American Journal of Physics 59 (2) (1991) 118–124.

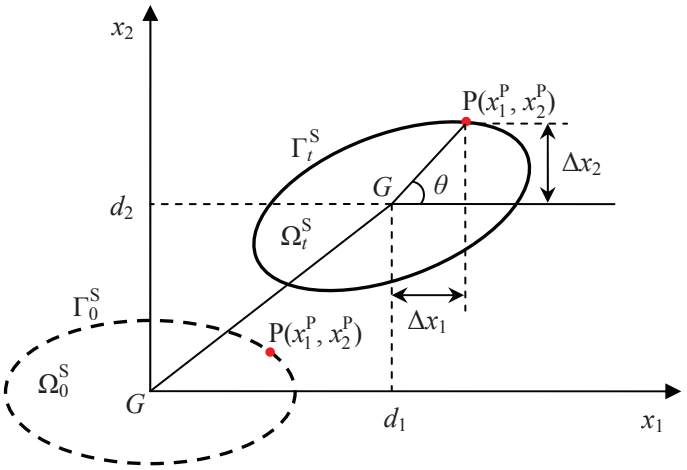

Fig. 1. Schematic view of the generalized 2D rigid-body motion

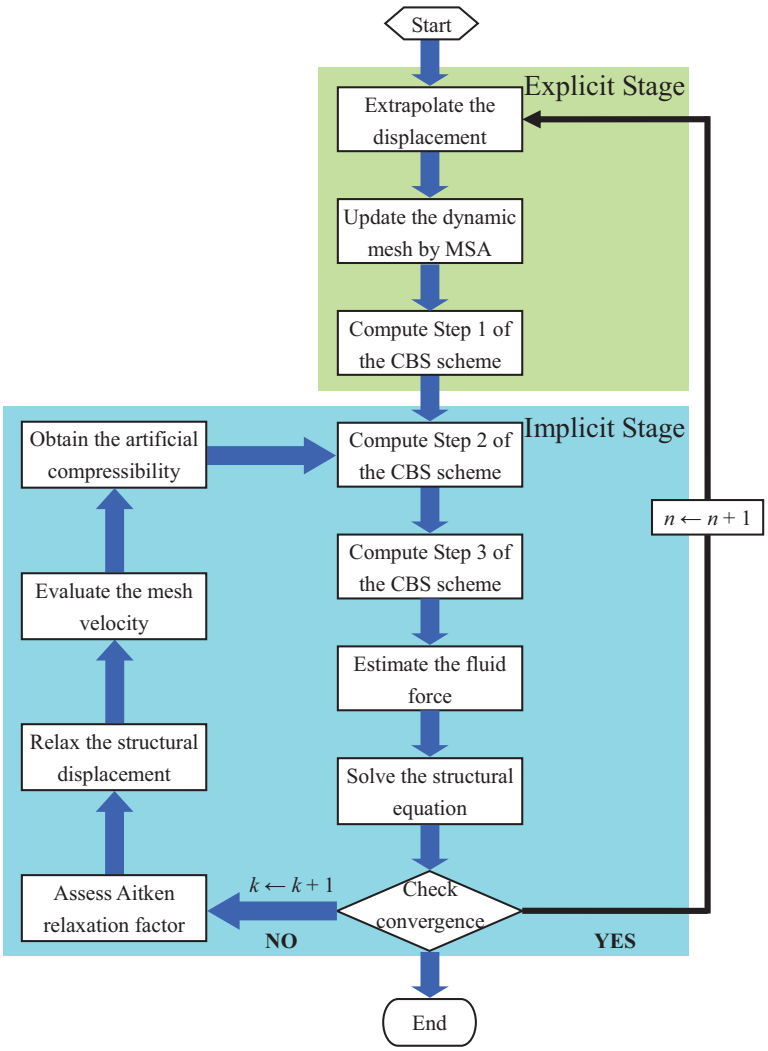

Fig. 2. Flowchart of the semi-implicit coupling algorithm

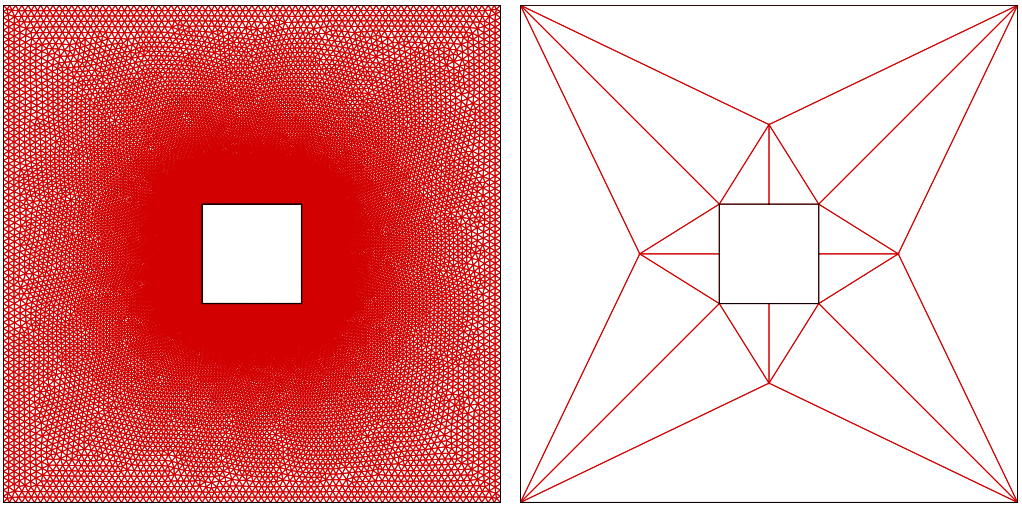

(a) System mesh

(b) Submesh with interior nodes (MSA-M1)

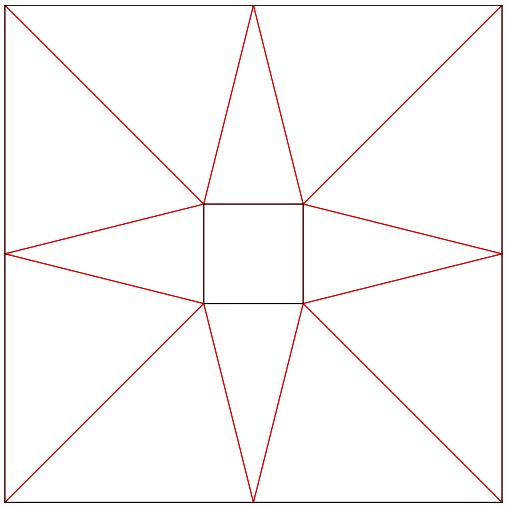

(c) Submesh without interior nodes (MSA-M2)

Fig. 3. The mesh updating test

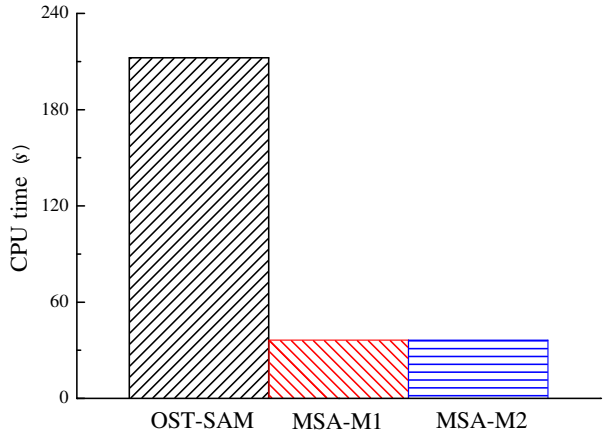

(a) CPU time

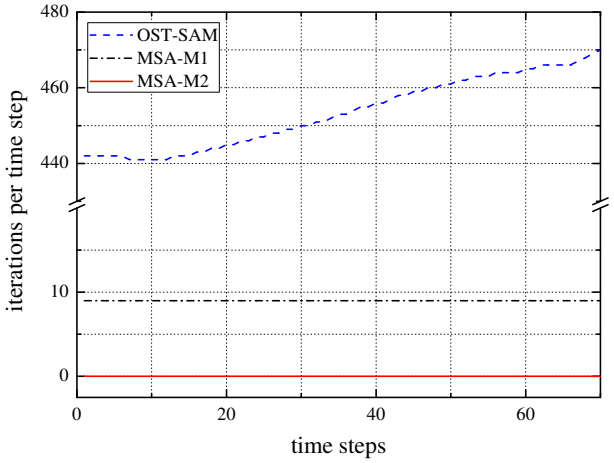

(b) Number of iterations

Fig. 4. Comparison of different mesh moving schemes

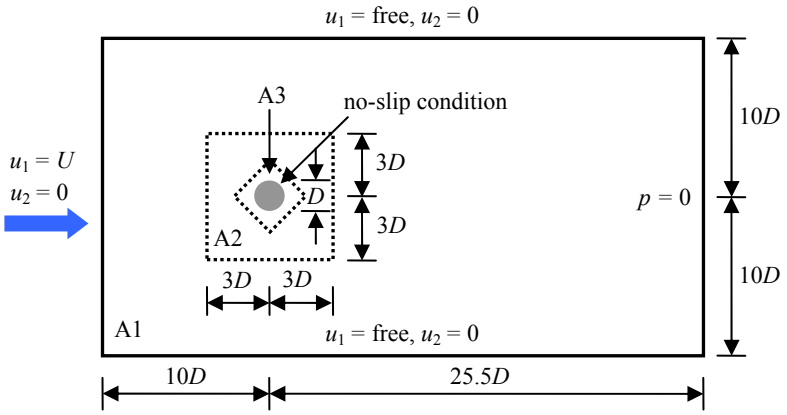

Fig. 5. Sketch of geometry and boundary conditions for the transversely oscillating circular cylinder

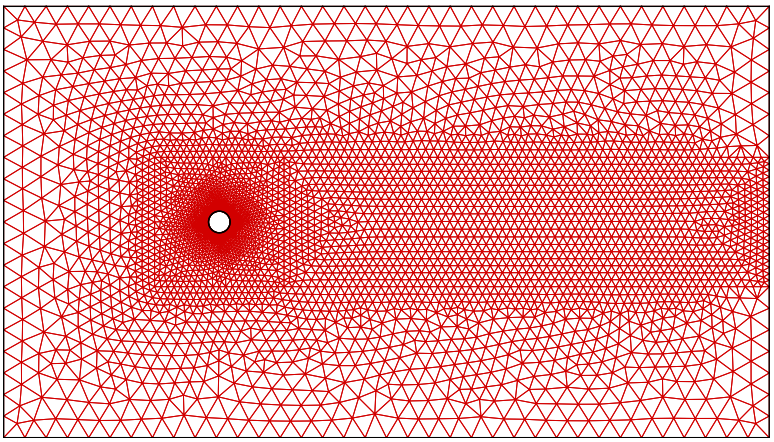

(a) Finite element mesh for the fluid field

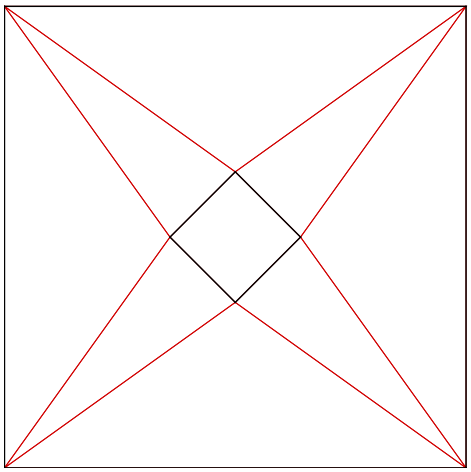

(b) MSA submesh for the ALE domain

Fig. 6. Mesh and submesh for the oscillating cylinder

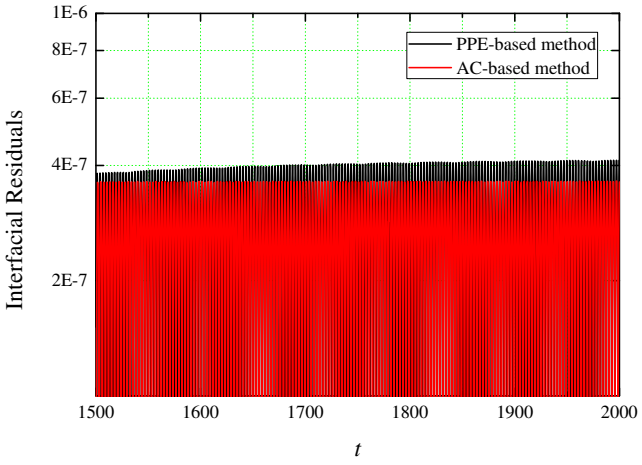

(a) Residual comparison

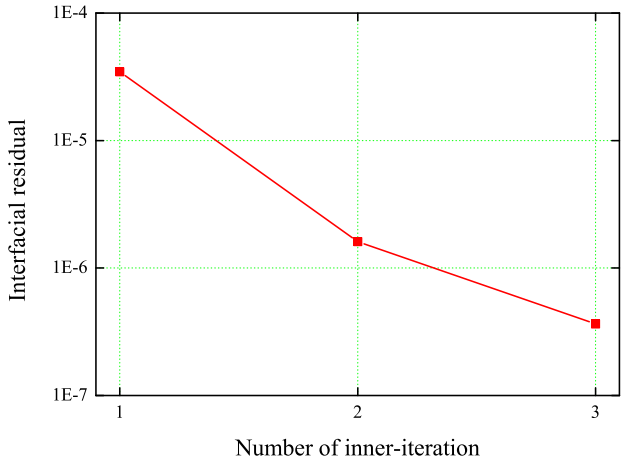

(b) Convergence history in a time step

Fig. 7. Convergence study for the $Re = 105$ flow

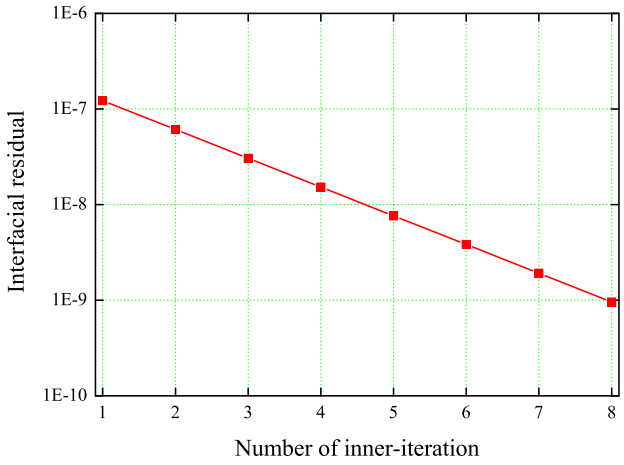

Fig. 8. Convergence plot for a time step using $tol = 1.0 \times 10^{-9}$

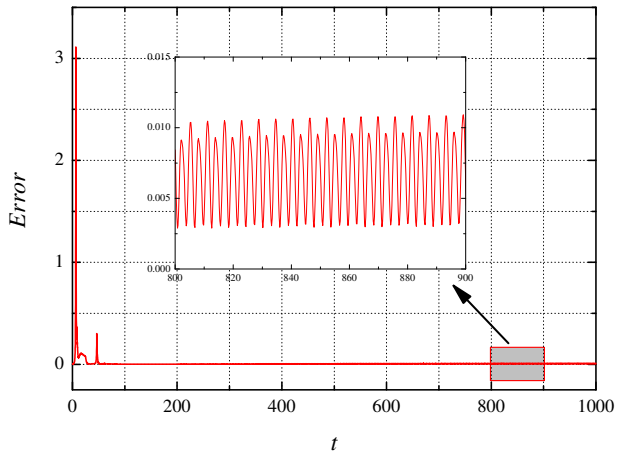

Fig. 9. Residual history of the modified continuity equation

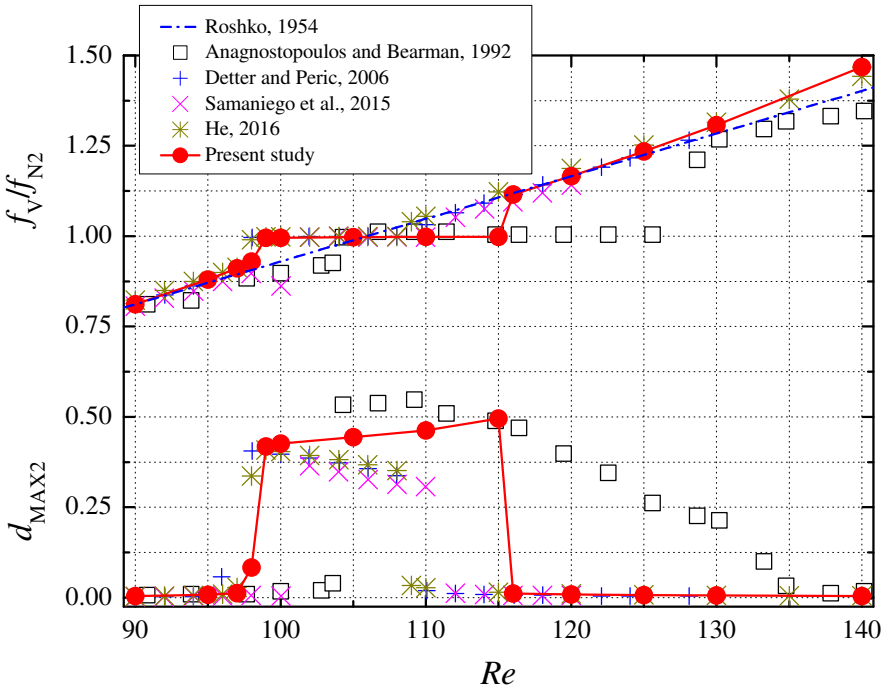

Fig. 10. Amplitude and frequency of the oscillating cylinder

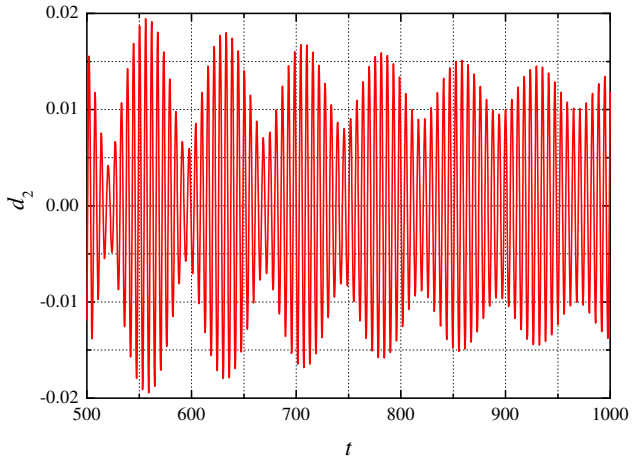

(a) $Re = 97$

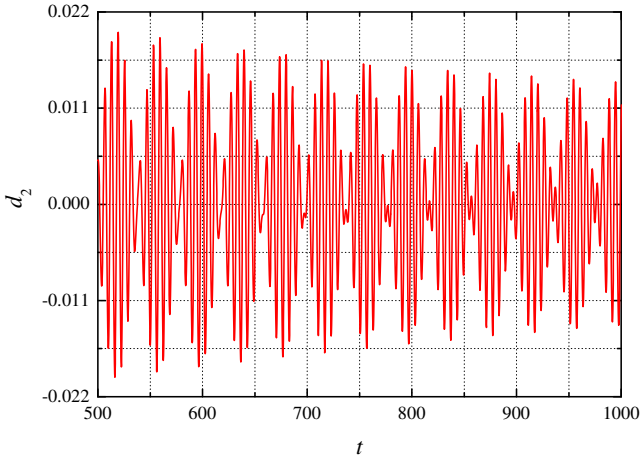

(b) $Re = 120$

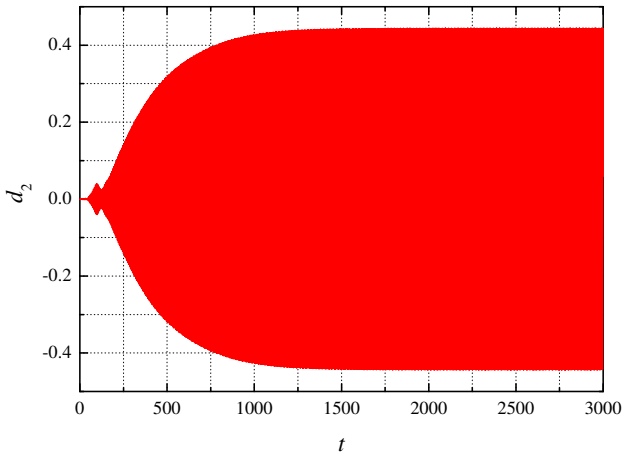

(c) $Re = 105$

Fig. 11. Time histories of the cylinder displacement at different Re

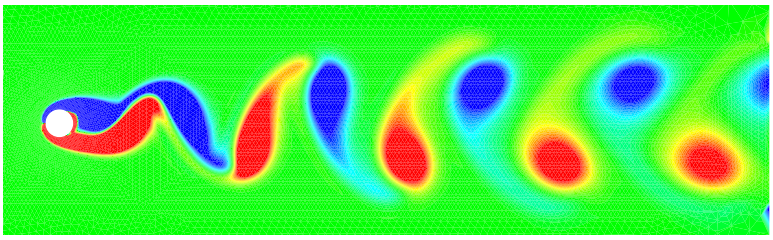

(a) $Re = 97$

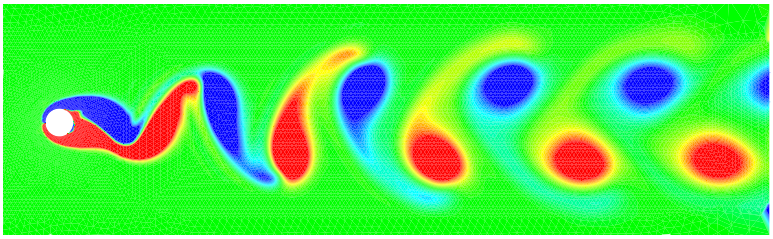

(b) $Re = 120$

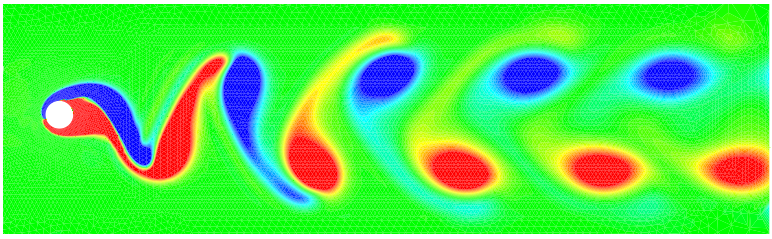

(c) $Re = 105$

Fig. 12. Vorticity contours of the oscillating cylinder at different Re

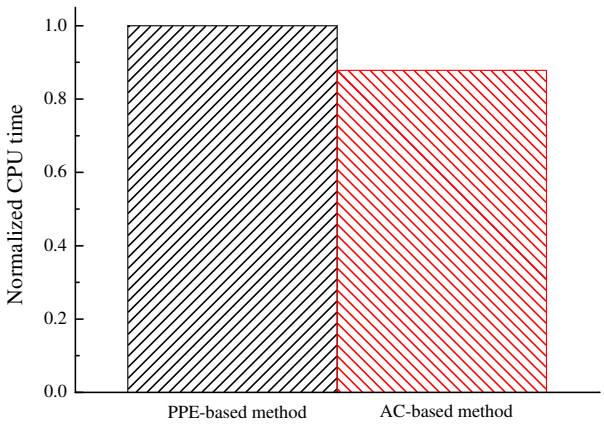

Fig. 13. Time consumption of two semi-implicit methods for the cylinder

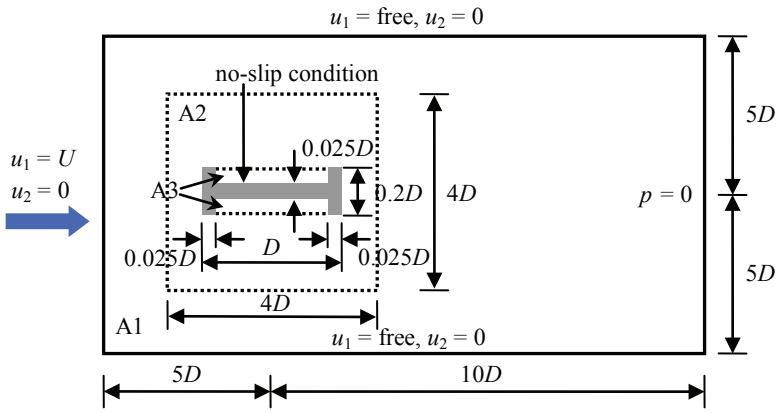

Fig. 14. Sketch of geometry and boundary conditions for the oscillating H-profile bridge deck

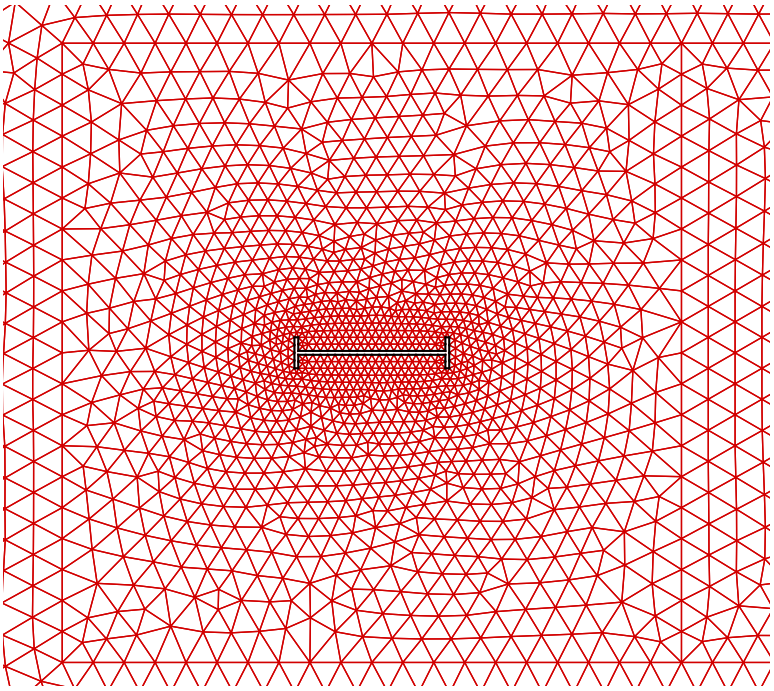

(a) Finite element mesh for the fluid field

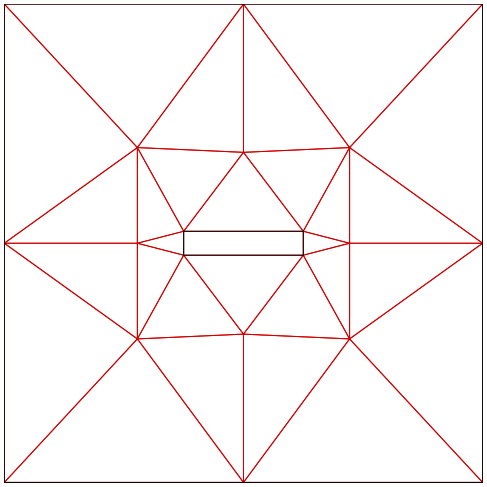

(b) MSA submesh for the ALE domain

Fig. 15. Mesh and submesh for the oscillating deck

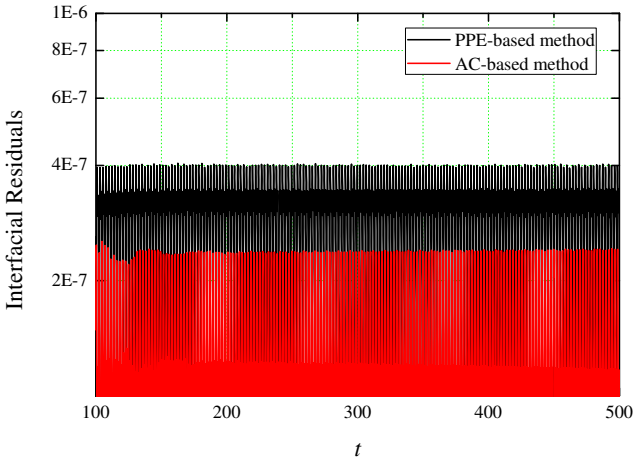

(a) Residual comparison

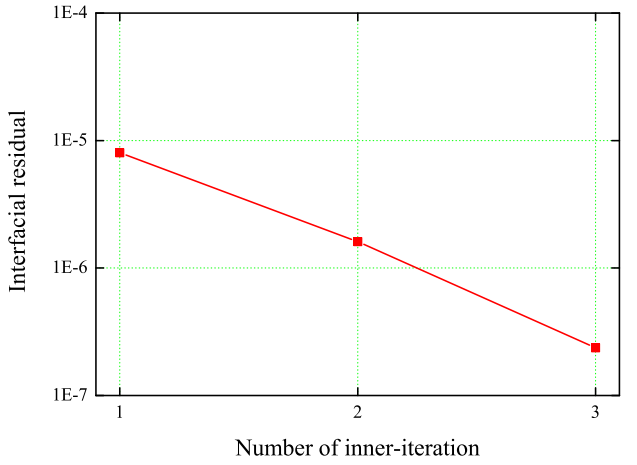

(b) Convergence history in a time step

Fig. 16. Convergence study for the deck problem

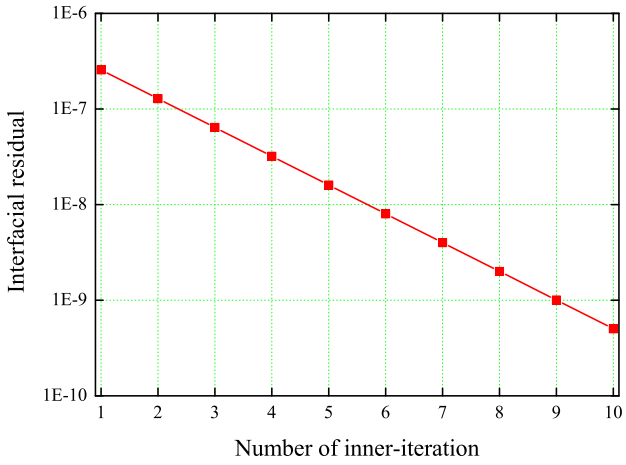

Fig. 17. Convergence plot for a time step using $tol = 1.0 \times 10^{-9}$

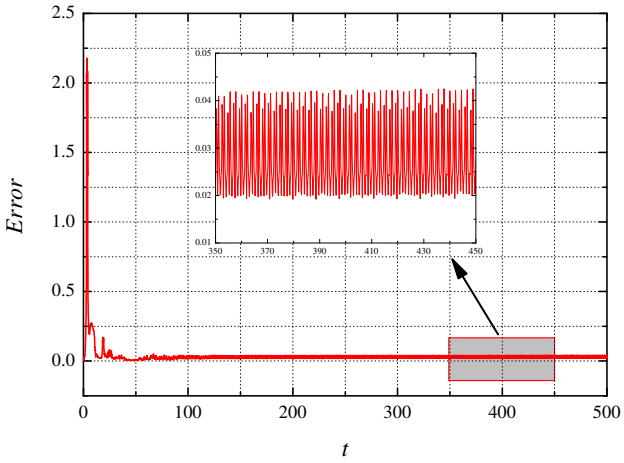

Fig. 18. Residual history of the modified continuity equation

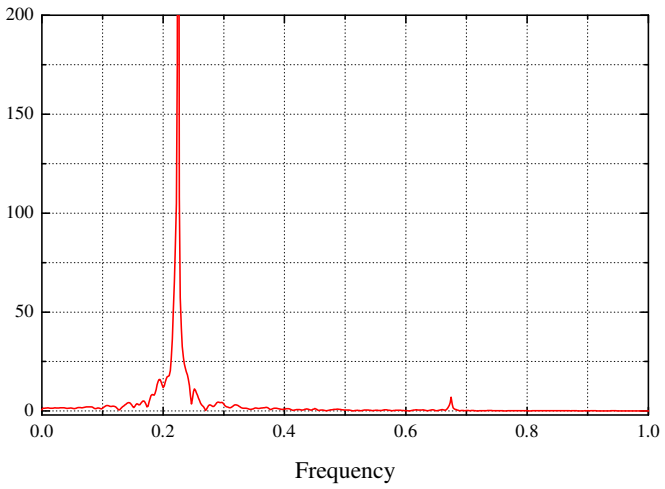

Fig. 19. Power spectra of the rotational time history

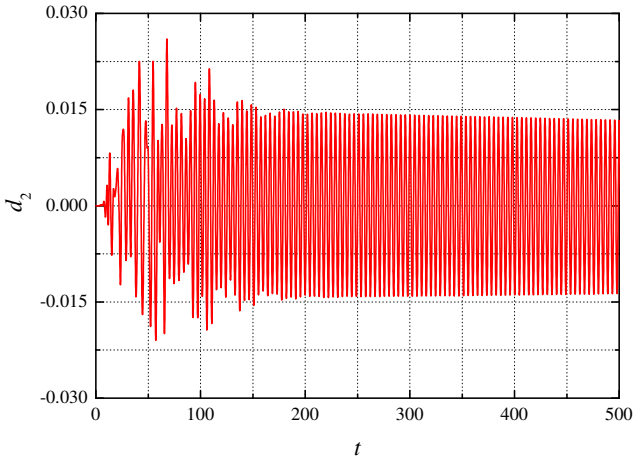

(a) Transverse displacement

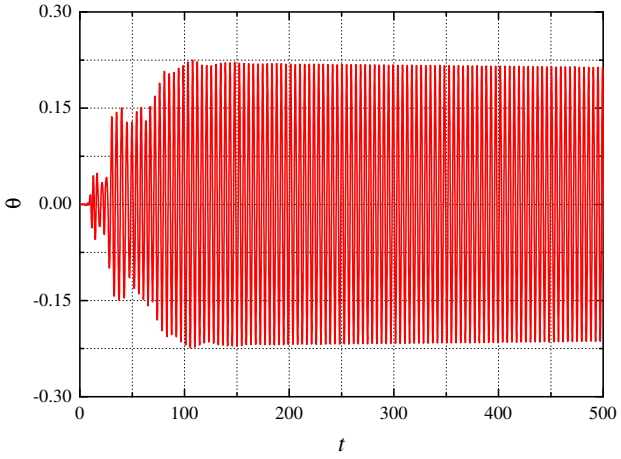

(b) Rotation

Fig. 20. Time histories of the oscillating deck

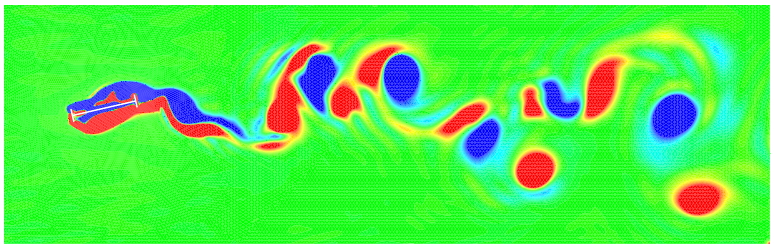

Fig. 21. Vorticity contour of the oscillating deck

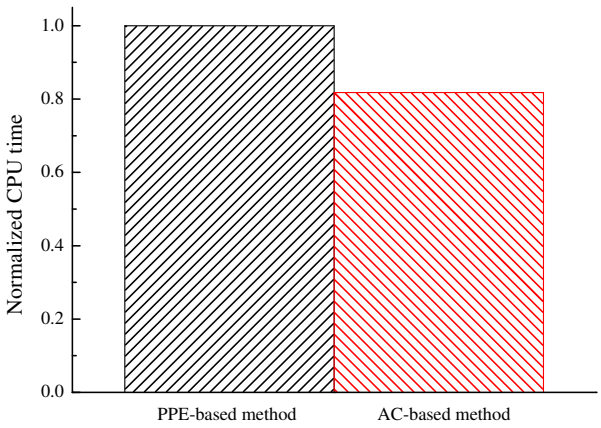

Fig. 22. Time consumption of two semi-implicit methods for the deck

Table 1. Effect of mesh resolution on the oscillating cylinder at $Re = 105$

Mesh	d_{MAX2}	$C_{\mathrm{D,MEAN}}$	$C_{\mathrm{D,RMS}}$	$C_{\mathrm{L,MAX}}$	$C_{\mathrm{L,RMS}}$	St	$f_{\mathrm{V}}/f_{\mathrm{N2}}$
M1	0.444	1.909	0.220	0.874	0.542	0.171	0.997
M2	0.446	1.921	0.215	0.800	0.540	0.171	0.997
Deviation	0.45%	0.63%	2.27%	8.47%	0.37%	0%	0%

Table 2. Effect of convergence tolerance on the $Re = 105$ flow

Tolerance	d_{MAX2}	$C_{\mathrm{D,MEAN}}$	$C_{\mathrm{D,RMS}}$	$C_{\mathrm{L,MAX}}$	$C_{\mathrm{L,RMS}}$	St
1.0×10^{-6}	0.444	1.909	0.220	0.874	0.542	0.171
1.0×10^{-9}	0.444	1.906	0.221	0.874	0.542	0.171

Table 3. Comparison of results for the oscillating cylinder at $Re = 100$

Reference	d_{MAX2}	St	$f_{\mathrm{V}}/f_{\mathrm{N2}}$
Dettmer and Perić [36]	0.397	0.179	0.999
Samaniego *et al.* [54]	0.0042	0.155	0.862
He *et al.* [6]	0.407	0.181	1.01
He [9]	0.405	0.179	0.998
Present study	0.426	0.179	0.998

Table 4. Effect of convergence tolerance on the oscillating deck

Tolerance	d_{MAX2}	f_{O2}	$d_{\mathrm{MAX}\theta}$	$f_{\mathrm{O}\theta}$
1.0×10^{-6}	0.0146	0.225	0.218	0.225
1.0×10^{-9}	0.0147	0.225	0.218	0.225

Table 5. Comparison of results for the oscillating deck

Reference	d_{MAX2}	f_{O2}	$d_{\mathrm{MAX}\theta}$	$f_{\mathrm{O}\theta}$
Filippini *et al.* [57]	0.0325-0.035	–	0.271	–
He [40]	0.0407	0.214	0.385	0.214
He [9]	0.0406	0.214	0.383	0.214
Present study	0.0146	0.225	0.218	0.225